# Gas-Liquid Flow around an Obstacle in a Vertical Pipe – CFD Simulation & Comparison to Experimental Data

Th. Frank(1), H.-M. Prasser(2), M. Beyer(3), S. Al Issa(3)

(1)ANSYS Germany, CFX Development
Staudenfeldweg 12, D-83624 Otterfing, Germany
Thomas.Frank@ansys.com
(2)ETH Zürich, Dept. Energy Technology, Zürich, Switzerland
(3)Forschungszentrum Dresden-Rossendorf (FZD), Institut of Safety Research, Rossendorf, Germany

**Keywords**: bubbly flows, CFD, wire-mesh sensor, 3-dimensional validation

## Abstract

A novel technique to study the two-phase flow field around an asymmetric diaphragm in a vertical pipe is presented, that allows to obtain detailed 3-dimensional data for CFD code validation in complex geometries. The investigated validation test case consists of an air-water two-phase bubbly flow around a half-moon shaped obstacle in a DN200 vertical pipe (TOPFLOW test facility), where the 3-dimensional flow field shows flow phenomena like curved stream lines, flow separation at sharp edges and recirculation zones in the obstacle wake, like they are common to complex flow situations in bends, T-junctions, valves, safety valves and other components of power plant and other industrial equipment. Pre-test calculations with the commercial flow solver ANSYS CFX have been performed using an Eulerian two-phase flow model with a monodisperse bubble diameter assumption and by taking into account all significant drag and non-drag forces contributing to the interphase momentum transfer. Results of the CFD simulation have been compared to the 3-dimensional air volume fraction and water velocity fields, which were obtained from the wire-mesh sensor data, where the comparison showed in general a very good agreement. Therefore CFD code validation on this type of complex 3-dimensional flow geometries permits the assessment of flow solver accuracy for other industrial type applications and contributes to further multiphase flow model development for ANSYS CFX.

## 1. Introduction

In the frame of the TOPFLOW project, vertical pipe flow is experimentally studied in order to develop and validate models for drag and non-drag forces acting on bubbles as well as for bubble coalescence and fragmentation in a gas-liquid two-phase flow. The advantage of TOPFLOW [1] consists in the combination of

(1) a large scale of the test channel (DN50 & DN200, approx. 9m height) with
(2) a wide operational range both in terms of the superficial velocities and the system pressure and finally
(3) the availability of an instrumentation that is capable in resolving structures of the gas-liquid interface, namely the wire-mesh sensors.

After a large number of experiments in straight vertical pipes [2-5], which are the basis of the development for a bubble size class model for ANSYS CFX (the so-called inhomogeneous MUSIG model, see [6-7]), the large test section with a nominal diameter of DN200 (Fig. 2) was used to study the flow field around an asymmetric obstacle (Fig. 1). This is an ideal test case for the CFD code and physical model validation before application to complex industrial flows, since the obstacle creates a pronounced three-dimensional two-phase flow field. Curved stream lines, which form significant angles with the gravity vector, a recirculation zone in the wake with buoyancy driven phase separation, a flow separation at the edge of the obstacle and its reattachment to the pipe walls are all phenomena widespread in real industrial components and installations. It has to be shown that the CFD-code predicts these phenomena well and accurate, after it has been equipped by new physical models, developed in simpler experimental geometries.

Recently, test series were performed with an air-water flow at ambient conditions as well as with a steam-water mixture at a saturation pressure of 6.5 MPa. Before the experiments were commissioned, an ANSYS CFX pre-test calculation was carried out for the air-water test 074, where flow conditions correspond to the bubbly flow regime. After the availability

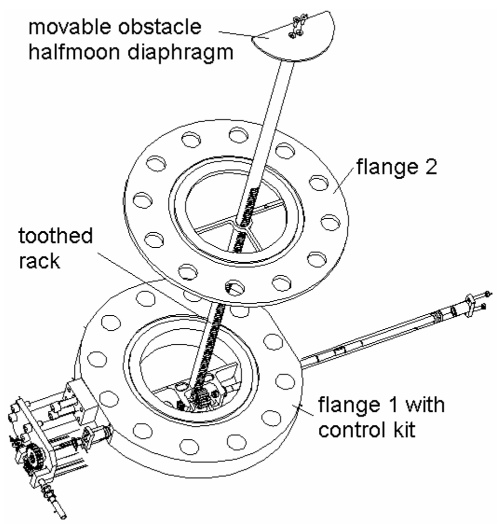


**Figure 1:** Movable obstacle with drive support for installation in TOPFLOW DN200 test section.

of the experimental data the CFD results have now compared in 3d and in very detail to the wire-mesh sensor data from the TOPFLOW test facility.

## 2. Nomenclature

| | |
|---|---|
| $C_L$ [-] | lift force coefficient |
| $C_{TD}$ [-] | turbulent dispersion force coefficient |
| $C_{WL}$ [-] | wall lubrication force coefficient |
| $C_{Wi}$ [-] | wall lubrication force coefficient of Antal's model (i=1,2) |
| $C_{W3}$ [-] | wall lubrication force coefficient of Tomiyama's model |
| $C_{Wi}$ [-] | wall lubrication force coefficient of Frank's model (i=D,C) |
| $d_H$ [m] | long axis of a deformable bubble |
| $d_P$ [m] | bubble diameter |
| D [m] | pipe diameter |
| $Eo$ [-] | Eötvös number |
| $\vec{F}_D \left[N \cdot m^{-3}\right]$ | drag force per unit volume |
| $\vec{F}_L \left[N \cdot m^{-3}\right]$ | lift force per unit volume |
| $\vec{F}_{WL} \left[N \cdot m^{-3}\right]$ | wall lubrication force per unit volume |
| $\vec{F}_{TD} \left[N \cdot m^{-3}\right]$ | turbulent dispersion force per unit volume |
| $k$ [m$^2$/s$^2$] | turbulence kinetic energy |
| L [m] | pipe length |
| $\vec{M}_i \left[N \cdot m^{-3}\right]$ | interfacial force term per unit volume |
| $\vec{n}_W$ [-] | wall normal vector |
| $p$ [Pa] | pressure |
| $r$ [-] | volume fraction |
| $\mathrm{Re}_P$ [-] | particle Reynolds number |
| $U$ [m/s] | velocity |
| $U_{rel}$ [m/s] | slip velocity |
| $y_W$ [m] | wall distance |

*Greek letters*

| | |
|---|---|
| $\varepsilon$ [m$^2$/s$^3$] | turbulence eddy dissipation |
| $\rho$ [kg/m$^3$] | density |
| $\nu$ [m$^2$/s] | kinematic viscosity |
| $\nu_t$ [m$^2$/s] | turbulent viscosity |
| $\mu$ [kg/m s] | viscosity |
| $\sigma$ [N/m] | surface tension |

*Subsripts*

| | |
|---|---|
| G | gaseous phase |
| L | liquid phase |
| norm | normalized |
| sup | superficial |
| t | turbulent |
| $\alpha$, $\beta$ | indices for continuous and disperse phase in a phase pair |

## 3. Experimental Facility

### 3.1. Test Arrangement and Measurement Technique

The test pipe of TOPFLOW has an inner diameter of 195.3 mm and a total height of 9 m (Fig. 2). Water is supplied from the bottom with a maximum flow rate of 50 kg/s. The two-phase flow is generated by feeding gas through an injector consisting of 16 radial tubes with a total number of 152 orifices of 0.8 mm diameter, connected to a conical head placed in the centre of the pipe (Fig. 3). The diaphragm (Fig. 1) is a half-moon shaped steel disk of 4mm thickness, the straight edge of which is arranged along the diameter of the pipe, while the circular edge is in a distance of 10 mm from the inner wall of the pipe. The disk is mounted on top of a toothed rod connected to a driving and translation mechanism to change the axial position of the diaphragm.

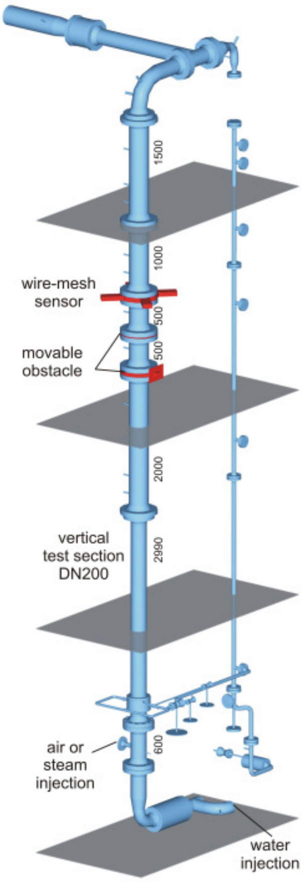


**Figure 2:** Vertical test section DN200 of TOPFLOW test facility at FZD with movable obstacle and wire-mesh sensor.

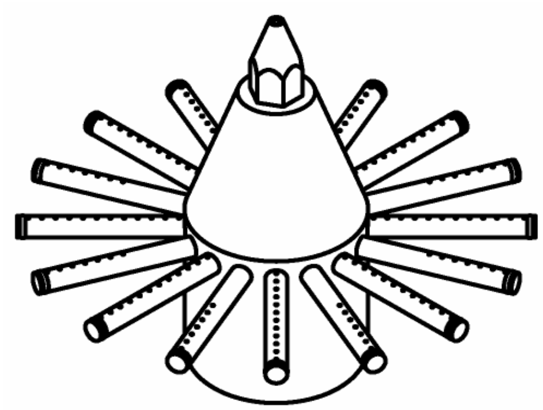

**Figure 3:** Sparger geometry used for gas injection.

Both obstacle and moving mechanism can be inverted and mounted either upstream or downstream of the wire-mesh sensor shown in Fig. 4. The sensor was located 6.17m downstream of the gas injection, when the asymmetric obstacle was put upstream of the sensor. When the obstacle was put downstream of the sensor, the distance was 5.11 m. Nevertheless it can be assumed, that in both cases and for different positions of the diaphragm the air-water bubbly flow arriving at the obstacle location is almost in fully developed flow condition.

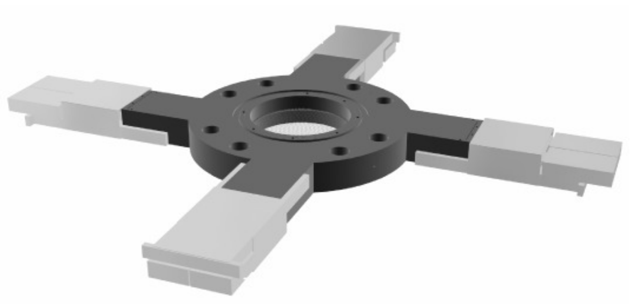

**Figure 4:** High-pressure wire-mesh sensor (DN200), measuring matrix of 64x64 points [8]

| superficial water velocity (m/s) \ superficial gas velocity (m/s) | 0.0368 | 0.0574 | 0.0898 | 0.14 | 0.219 | 0.342 | 0.534 | 0.835 |
|---|---|---|---|---|---|---|---|---|
| 1.611 | 075 | 086 | 097 | 108 | 119 | 130 | 141 | 152 |
| 1.017 | 074 | 085 | 096 | 107 | 118 | 129 | 140 | 151 |
| 0.405 | 072 | 083 | 094 | 105 | 116 | 127 | 138 | 149 |
| 0.102 | 069 | 080 | 091 | 102 | 113 | 124 | 135 | 146 |

**Figure 5:** Test matrix; grey fields are test points for air-water and steam-water flow tests

The described arrangement allows acquisition of local instantaneous void fractions from the full cross-section of the pipe with a spatial resolution of 3 mm and a rate of 2.5 kHz within the 3-dimensional flow field around the diaphragm. The distance between sensor and diaphragm can be varied from 10 mm to a maximum distance of 520 mm without moving the sensor position, which is essential to perform high-pressure experiments in an efficient way, i.e. without dismantling and rearranging the test facility each time the measuring position has to be changed.

### 3.2. Experimental Test Parameters

Measurements were carried out with an air-water flow at ambient pressure and a temperature of 25 °C as well as with a steam-water mixture under saturation conditions at 6.5 MPa for the superficial velocities shown in Fig. 5. The following distances between diaphragm and mesh sensors were realized: $\Delta z = \pm520, \pm250, \pm160, \pm80, \pm40, \pm20, \pm15, \pm10$mm, where the positive coordinate direction refers to measurement locations downstream of the diaphragm. Wire-mesh sensor signals were recorded after achieving a steady state for a measuring period of 10 s for each combination of boundary conditions. For each realized combination of superficial velocities data from both air and steam tests are available. Finally for each of the tests 3-dimensional field values of the gas volume fraction and the module of the vertical water velocity component are available. Furthermore from the wire-mesh sensor data the local bubble size distribution at each measurement location can be derived. In order to compare the 3-dimensional data fields of gas void fraction and absolute water velocity with the CFD results, the data were imported into the ANSYS CFX graphical post-processor. This approach allowed the application of identical data processing, data extraction (e.g. lines, cutting planes and isosurfaces) and color schemes and therefore a more direct comparison of the CFD results and experimental data. Since experimental data have a fine (64×64) planar resolution in the x-y-plane but a limited and with increasing distance to the diaphragm substantially coarser resolution in z-direction due to the distance of the measuring planes, a pre-interpolation of the experimental data in z-direction has been applied with an axial resolution of the interpolated data of $\Delta z$=1mm in the range between $-520\text{mm} \leq z \leq +520\text{mm}$.

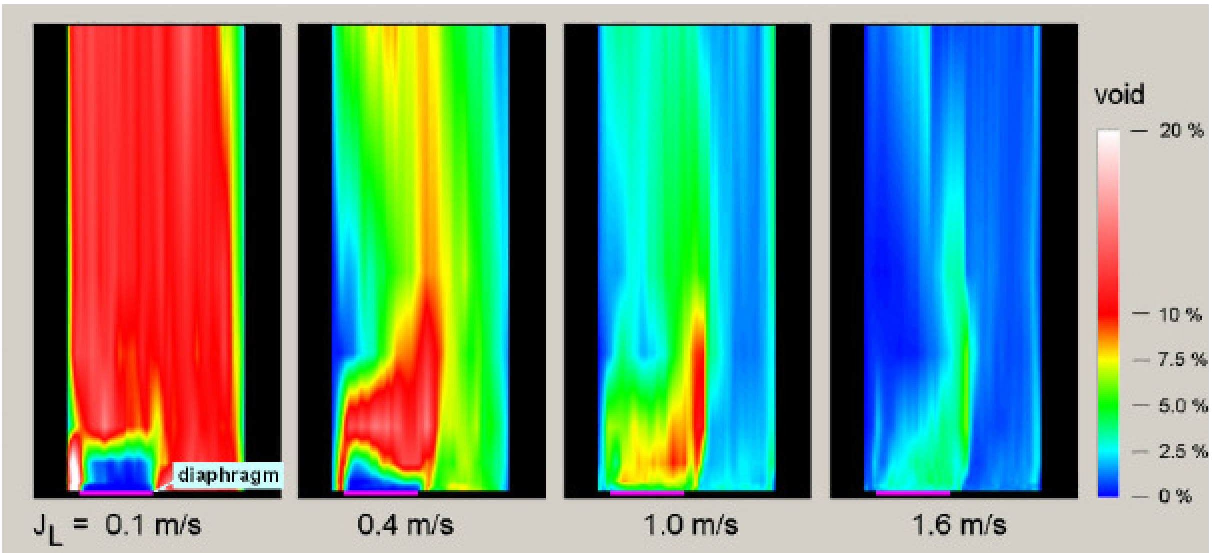


**Figure 6:** Change of measured void fraction profiles downstream of the diaphragm at $J_G$ = 0.037 m/s with a variation of the superficial liquid velocity $J_L$.

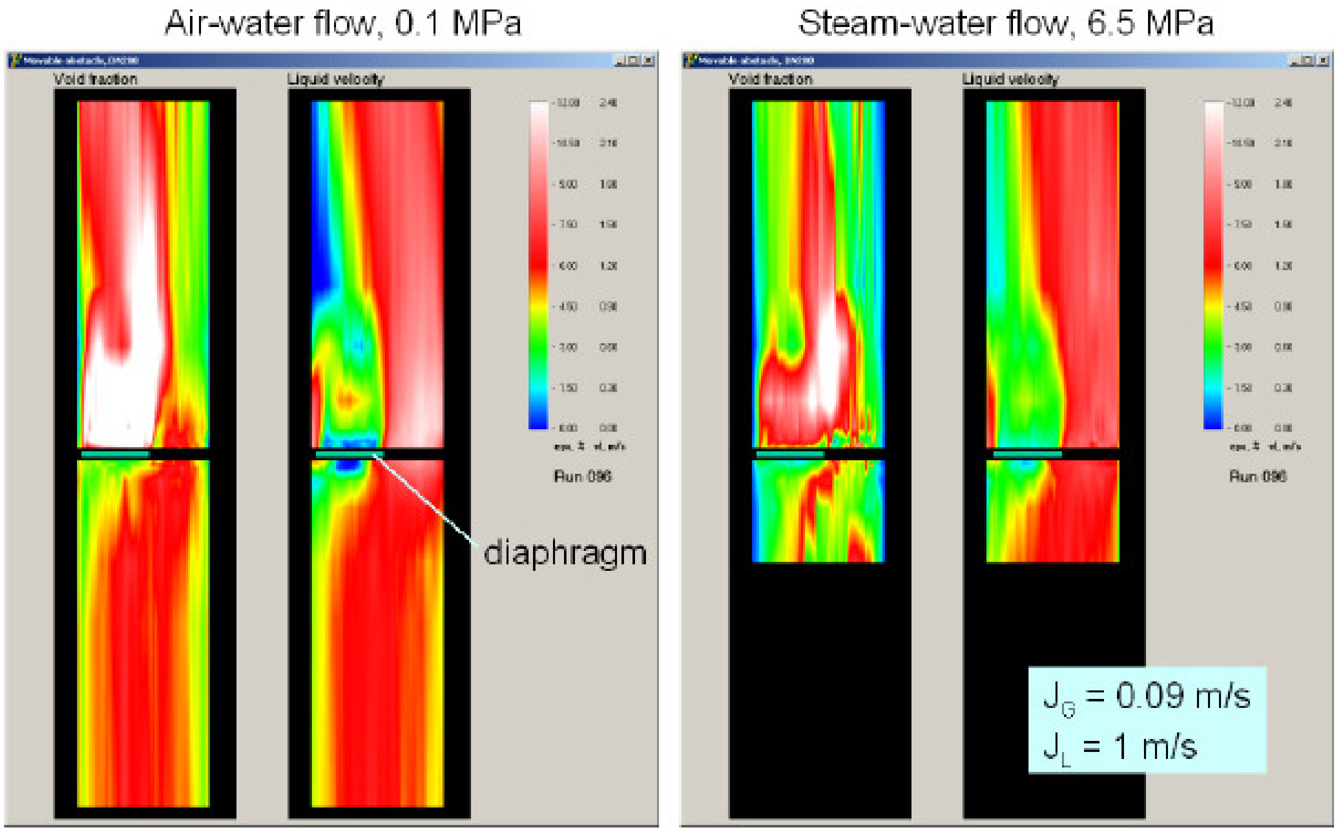


**Figure 7:** Void fraction and absolute liquid velocity profiles in an air-water and a steam-water test at identical superficial gas and liquid velocities $J_G$ and $J_L$.

### 3.3. Experimental Results

The wire-mesh sensor data were used to calculate two-dimensional time-averaged void fraction distributions in the measuring plane. By combining the information from measurements with different distances between sensor and diaphragm, full three-dimensional void distributions around the obstacle were obtained. A centre cut along the axis of the test pipe in a vertical plane perpendicular to the straight edge of the half-moon diaphragm is a very illustrative way to visualize the void fraction field. This was done in Fig. 6 for the field downstream of the diaphragm. At small superficial water velocities, there is a region free of bubbles directly behind the obstacle, which vanishes with increasing water velocity. The wake, i.e. the zone where a distortion of the void field is found, grows in downstream direction with increasing liquid velocity, while the overall void fractions naturally decrease.

There is a way to assess time-averaged local liquid velocities by evaluating the transit time of bubbles of a certain range of diameters. Due to the spatial resolution, the sensor data can be used to determine the lateral extension of each individual bubble by measuring the maximum area occupied by the bubble within the measuring plane during its passage [2,8]. If a spherical bubble shape can be assumed, the diameter of a circle with an equivalent area divided by the time of the passage reveals the bubble velocity. A local instantaneous value of the liquid velocity is available after subtracting the bubble rise velocity. Time-averaged profiles of the absolute axial liquid velocity are calculated by averaging individual values from a manifold of analysed bubbles. Bubble deformation causes a systematic error that has to be eliminated by a calibration procedure.

In order to keep the bubble deformation and the bubble rise velocity in a narrow band, velocities are calculated only from bubbles of a certain bubble size interval, which was set to 4-5 mm, so-called "marker bubbles". It was assumed that the bubble deformation can be accounted for by a calibration factor of the individual bubble velocity. This factor is determined by integrating the velocity profile found under the assumption of spherical bubbles over the cross-section and comparing the result with the known liquid superficial velocity. Examples are shown in Fig. 7, where the results of both air and steam experiments executed at identical superficial velocities are shown.

The velocity field indicates a recirculation zone behind the obstacle. It has to be kept in mind that the marker bubble method cannot supply information on the sign of the axial liquid velocity. Negative values expected in the centre of the recirculation zone can therefore not be reproduced and a local maximum is found instead.

By the estimation of liquid velocity profiles it becomes clear that the high gas fractions in the wake of the obstacle are caused by entrapping bubbles in the recirculation zone. On the other hand, upstream of the diaphragm the expected stagnation point is nicely reproduced and the concentration of the gaseous phase is decreased. In the free cross-section area aside of the obstacle both the liquid velocity and gas volume fraction show maxima.

Concerning the general structure of the two-phase flow field, no large qualitative differences were found between the air-water and the steam-water experiment. The void fractions and the velocities are smaller in case of the high-pressure tests. The recirculation zone is less pronounced in the steam-water experiment.

## 4. Physical Model and Setup of CFD Simulations

Before the experiments were commissioned, a pre-test calculation was carried out for the boundary conditions of the air-water test 074, which was performed at the superficial velocities $J_L$ = 1.0 m/s and $J_G$ = 0.037 m/s. The flow conditions for this test correspond to the bubbly flow regime with a comparable small amount of bubble breakup and coalescence. Therefore for the CFD simulation with ANSYS CFX the Eulerian two-phase flow model was used, which is outlined below.

### 4.1. The Physical Model

Based on previous observations for the test conditions 074 for straight pipe tests at TOPFLOW and MT-Loop [6,15,16] the bubbly two-phase flow was assumed to be monodisperse. Consequently the blind pre-calculations of the gas-liquid monodispersed bubbly flow in the test geometry was based on the ANSYS CFX multi-fluid Euler-Euler approach [10]. The applied Eulerian modeling framework is based on ensemble-averaged mass and momentum transport equations for all phases, where the number of contemporary solved phase transport equations is only limited by computational ressources. Regarding the liquid phase as continuum ($\alpha$=L) and the gaseous phase as disperse bubbles ($\alpha$=G) these equations for a monodisperse two-phase flow read:

$$\frac{\partial}{\partial t}\left(r_\alpha \rho_\alpha\right)+\nabla.\left(r_\alpha \rho_\alpha \vec{U}_\alpha\right)=0 \tag{1}$$

$$\begin{aligned}\frac{\partial}{\partial t}\left(r_\alpha \rho_\alpha \vec{U}_\alpha\right)+\nabla.\left(r_\alpha \rho_\alpha \vec{U}_\alpha \otimes \vec{U}_\alpha\right)= \\ \nabla.\left(r_\alpha \mu_\alpha (\nabla \vec{U}_\alpha+(\nabla \vec{U}_\alpha)^T)\right)-r_\alpha \nabla p \\ +r_\alpha \rho_\alpha \vec{g}+\vec{M}_\alpha\end{aligned} \tag{2}$$

$$\vec{M}_\alpha=\vec{F}_D+\vec{F}_L+\vec{F}_{WL}+\vec{F}_{TD} \tag{3}$$

where $r_\alpha$, $\rho_\alpha$, $\mu_\alpha$ are the void fraction, density and viscosity of the phase $\alpha$ and $\vec{M}_\alpha$ represents the sum of interfacial forces like the drag force $\vec{F}_D$, lift force $\vec{F}_L$, wall lubrication force $\vec{F}_{WL}$ and turbulent dispersion force $\vec{F}_{TD}$. Turbulence of the liquid phase has been modeled using Menter's k-$\omega$ based Shear Stress Transport (SST) model [10]. The turbulence of the disperse bubbly phase was modeled using a zero equation turbulence model and bubble induced turbulence has been taken into account according to Sato's model [10].

The interfacial drag and non drag force terms $M_\beta$ can be written as:

$$\vec{F}_D=\frac{3}{4}C_D\frac{r_\beta \rho_\alpha}{d_\beta}\left|\vec{U}_\alpha-\vec{U}_\beta\right|(\vec{U}_\alpha-\vec{U}_\beta) \tag{4}$$

$$\vec{F}_L=C_L r_\beta \rho_\alpha(\vec{U}_\alpha-\vec{U}_\beta)\times\nabla\times\vec{U}_\alpha \tag{5}$$

$$\vec{F}_{WL}=-C_{WL} r_\beta \rho_\alpha\left|\vec{U}_{rel}-(\vec{U}_{rel}\cdot\vec{n}_W)\vec{n}_W\right|^2\vec{n}_W \tag{6}$$

and according to the RPI turbulent dispersion force model:

$$\vec{F}_{TD}=-C_{TD}\rho_L k_L \nabla r_G \tag{7}$$

or using the Favre-averaged-drag (FAD) turbulent dispersion force model formulation [ 6,11]:

$$\vec{F}_{TD}=D_{\alpha\beta}A_{\alpha\beta}\frac{\nu_{t\alpha}}{\sigma_{r\alpha}}\left(\frac{\nabla r_\alpha}{r_\alpha}-\frac{\nabla r_\beta}{r_\beta}\right) \tag{8}$$

Here $\alpha$ denotes the liquid phase and $\beta$ the properties of the gaseous phase of the corresponding phase pair. These interfacial momentum transfer terms need further closure relations for the various force coefficients $C_D$, $C_L$, $C_{WL}$, $C_{TD}$ and model parameters like $\sigma_{r\alpha}$. In the present study the Grace drag law [10], Tomiyama lift force coefficient [12] and the so-called Favre-averaged-drag (FAD) turbulent dispersion model [6,11] were used. The high gas void fraction correction exponent in the Grace drag law was set to n=4 as recommended for gas-liquid flows. The lift force coefficient $C_L=C_L(\mathrm{Eo}_d)$ has been determined in accordance with the correlation for deformable bubbles published by Tomiyama [12] as a function of the bubble Eötvös number:

$$C_L=\begin{cases}\min\left[0.288\tanh(0.121\mathrm{Re}_P),f(Eo_d)\right], & Eo_d<4\\ f(Eo_d), & 4\le Eo_d\le 10\\ -0.27, & Eo_d>10\end{cases} \tag{9}$$

with:

$$\begin{aligned}f(Eo_d)=0.00105Eo_d^3-0.0159Eo_d^2\\ -0.0204Eo_d+0.474\end{aligned} \tag{10}$$

where $Eo_d$ is the Eötvös number based on the long axis $d_H$ of a deformable ellipsoidal shaped bubble, i.e.:

$$\begin{aligned}Eo_d&=\frac{g\left(\rho_L-\rho_G\right)d_H^2}{\sigma}\\ d_H&=d_P(1+0.163Eo^{0.757})^{1/3}\\ Eo&=\frac{g\left(\rho_L-\rho_G\right)d_P^2}{\sigma}\end{aligned} \tag{11}$$

The given correlation of eq. (9) takes into account bubble deformation and asymmetric wake effects on bubble lift and leads to a sign change of the lift force for bubbles with a diameter of $d_P>5.5mm$ for air bubbles in water under normal conditions. The critical bubble diameter, where the sign change of the lift force occurs, strongly depends on the bubble surface tension and shifts towards smaller bubble diameters of about $d_P\sim 3.5mm$ for e.g. a vapor-water system under higher pressure of about 65bar and at saturation temperature. The bubble size dependent bubble lift force leads further to the fact, that in a polydisperse bubbly flow bubbles of different diameter tend to separate. This bubble separation effects cannot be described in the framework of a monodisperse, fixed bubble diameter two-phase flow model with a single gaseous phase velocity field. The inhomogeneous MUSIG model [6,7] has been developed for ANSYS CFX in order to take into account such bubble separation effects induced by the bubble lift force in dependence on the bubble size distribution. For future prediction of test case conditions other then 074 at higher gas volume fractions it will be of importance to take these bubble separation effects as well as bubble breakup and coalescence into account.

For the wall lubrication force model the formulation of Antal [14]:

$$C_{WL} = \max\left\{0, \frac{C_{W1}}{d_P} + \frac{C_{W2}}{y_W}\right\} \tag{12}$$

with $y_W$ being the wall distance and recommended values of $C_{W1}$=-0.01 and $C_{W2}$=0.05 as well as the formulation of Tomiyama [13]:

$$C_{WL} = C_{W3}\frac{d_P}{2}\left(\frac{1}{y_W^2} - \frac{1}{(D-y_W)^2}\right) \tag{13}$$

with D being the pipe diameter and:

$$C_{W3} = \begin{cases} e^{-0.933Eo+0.179} & 1 \le Eo \le 5 \\ 0.00599Eo - 0.0187 & 5 < Eo \le 33 \\ 0.179 & 33 < Eo \end{cases} \tag{14}$$

have been developed. From validation simulations for straight pipe flows it could be shown, that both formulations of Antal and Tomiyama have disadvantages [6]. While the Antal formulation is geometry independent, it can be shown from numerical simulations that the formulation fails under certain flow conditions because the wall lubrication force predicted by eq. (6) and (12) is too small in order to balance strong lift forces arising from eq. (5). The Tomiyama formulation for the wall lubrication force from eq. (6), (13) and (14) leads to improved prediction of gaseous phase volume fraction profiles for a wider range of flow conditions. But the formulation is limited to pipe flow investigations since it contains the pipe diameter as a geometry length scale. In order to derive a geometry independent formulation for the wall lubrication force while preserving the general behavior of Tomiyama's formulation, Frank [7] supposes a generalized formulation for the wall lubrication force as follows:

$$C_{WL} = C_{W3}(Eo) \cdot \max\left\{0, \frac{1}{C_{WD}} \cdot \frac{1 - \frac{y_W}{C_{WC} d_P}}{y_W \cdot \left(\frac{y_W}{C_{WC} d_P}\right)^{p-1}}\right\} \tag{15}$$

with the cut-off coefficient $C_{WC}$, the damping coefficient $C_{WD}$ and a variable potential law for $F_{WL} \sim 1/y_W^p$. The Eötvos number dependent coefficient $C_{W3}(Eo)$ is determined from eq. (14) preserving the dependency on bubble surface tension. From numerical simulations it was found, that a good agreement with experimental data can be obtained for $C_{WC}$=10.0, $C_{WD}$=6.8 and p=1.7. Thereby the introduction of an additional geometrical length scale can be avoided, which is difficult to be correctly defined in arbitrary geometries.

### 4.2. Flow Geometry and Numerical Meshes

Flow geometry for the movable obstacle including support and drive mechanism as shown in Fig. 1 had been supplied as CAD data by FZD, but for the blind pre-test CFD simulations the geometry had been simplified to a large extent. Finally the air-water two-phase flow around the obstacle was simulated on hexahedral meshes created with ICEM-CFD Hexa and consisting of about 119.000 and 473.000 hexahedral mesh elements. Furthermore mesh independency of results was checked for single-phase flow on an even finer mesh with 3.739.000 mesh elements.

Meshes were generated for half of the TOPFLOW geometry assuming axial symmetry at the midplane of the pipe. The flow geometry for the CFD simulation therefore consisted of 1.5m pipe sections up- and downstream of the obstacle (D=198mm), the obstacle geometry with its finite thickness of 4mm located at z=0mm and its gap width to the outer pipe wall of 10mm. The geometrical details of the drive and support mechanism were neglected. This geometry simplification is well satisfied for the comparison of CFD results with upstream flow measurements (z=-10mm to z=-520mm), since in this case the drive and support mechanism was located downstream of the wire-mesh sensor and the obstacle. In case of the data comparison for measurement cross-sections downstream of the obstacle (z=+10mm to z=+520mm) some flow disturbances from the upstream located support mechanism and resulting influence on the flow and phase distribution downstream of the obstacle should be expected, also it was not quantified.

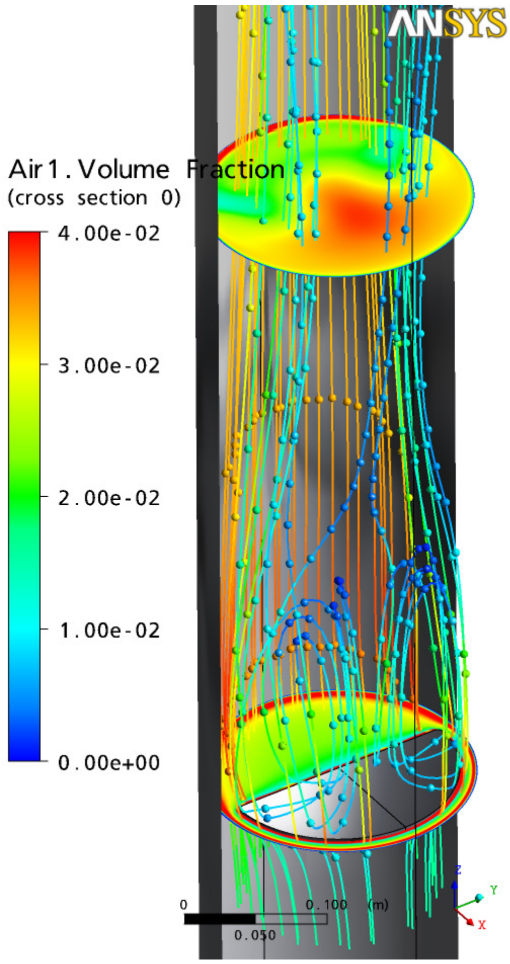


**Figure 8:** Streamlines around the movable obstacle.

### 4.3. Model Setup and Boundary Conditions for the CFD Simulation

Before the experiments were commissioned a steady-state pre-test calculation was set-up for the flow conditions of the air-water test 074, which was performed at the superficial velocities $J_L$ = 1.0 m/s and $J_G$ = 0.037 m/s. Test conditions of this air-water test 074 correspond to ambient pressure and temperature of 25°C and the flow morphology corresponds to the bubbly flow regime.

For the CFD simulation using ANSYS CFX the Eulerian two-phase flow model as outlined in section 4.1 was used

[6,10], where both phases were treated as non-compressible fluids. Further it was assumed that the gaseous phase consists of monodisperse bubbles. In correspondence with the sparger characteristics a bubble diameter of $d_P$=4.8mm was prescribed at the inlet. In order to account for the hydrostatic bubble expansion with increasing pipe elevation, a linearly dependent equivalent bubble diameter $d_P$=$d_P(z)$ in the range of 4.8-5.2mm was used. Bubble drag in accordance to Grace drag law, Tomiyama lift force, Frank's generalized wall lubrication force, the FAD turbulent dispersion force and the Sato model for bubble induced turbulence have been taken into account [6,10]. Bubble coalescence and fragmentation were neglected for this first pre-test simulation, also it can be assumed that bubble fragmentation will take place at the edges of the obstacle and coalescence might become of importance in regions of bubble accumulation i.e. in the wake behind the obstacle.

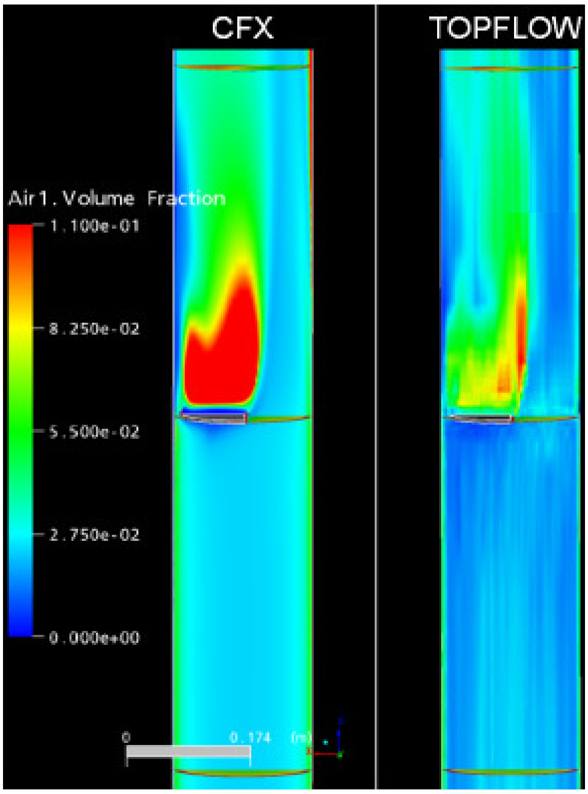


**Figure 9:** Comparison between experiment (right) and CFX result (left) for air volume fraction distribution in the symmetry plane of the flow geometry for -500mm≤z≤500mm.

Restriction of the flow geometry to L=1.5m upstream of the obstacle allowed only for flow development from inlet boundary conditions over a distance of L/D~7.5, while in the experiments the sparger was located far upstream the movable obstacle (L/D~30). Therefore the inlet boundary conditions were set to fully developed two-phase pipe flow profiles for air and water velocities, radial gas volume fraction distribution, turbulent kinetic energy and turbulent eddy frequency. These profile data were obtained from a previously performed flow simulation for a 8.5m long vertical pipe flow under test case 074 conditions in a D=198mm pipe without the obstacle (TOPFLOW geometry) and therefore saving substantial computational effort for the intended CFD simulations for the flow around the movable obstacle on differently refined meshes. At the outlet cross section of the 3.0m long pipe section an averaged static pressure outlet boundary condition was used. Symmetry boundary condition was applied to the midplane of the geometry at y=0. Wall boundary conditions at the pipe wall and the obstacle surface were set to a non-slip boundary condition for the continuous phase and a free slip boundary condition for the disperse phase. ANSYS CFX automatic wall treatment was used for the SST turbulence model for turbulence prediction of the continuous phase, while a zero equation disperse phase turbulence model was applied for the turbulence modelling of the disperse gaseous phase [10].

## 5. Results and Discussion

Results of ANSYS CFX steady-state pre-test calculations on the mesh with 473.000 mesh elements have well produced all qualitative details of the structure of the two-phase flow field around the movable obstacle for test conditions 074. From streamlines around the obstacle shown in Fig. 8 it can be observed, that a large recirculation zone is predicted downstream of the obstacle. Shape, extension and the reattachment length of this recirculation zone fairly well correspond to the experimental observations.

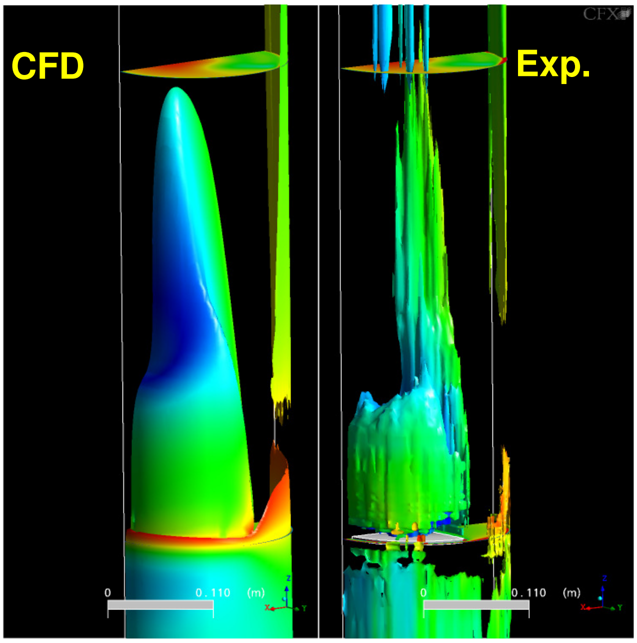


**Figure 10:** Comparison of isosurfaces for experimental data and CFD result at 4% air volume fraction. Colour corresponds to local fluid velocity.

The vortex flow in the wake behind the obstacle leads to bubble entrainment and air void fraction accumulation in this recirculation zone as can be seen from Fig. 9 and Fig. 10. The plot of the air void fraction at the symmetry plane of the geometry for both the CFD result and experimental data has been obtained by the import of pre-interpolated experimental data into the ANSYS CFX postprocessor, as outlined in section 3.2. The direct data comparison shows, that the shape and the extension of the higher air void fraction region in the wake of the obstacle is quite comparable, also in the CFD simulation higher air volume fractions of up to 15% are reached in the vortex core, which can not be observed in the experiment. An explanation for this discrepancy between CFD result and experimental data can be found in the underlying CFD model assumption of a prescribed and locally constant bubble diameter. In the experiment the air entrainment and accumulation in the vortex behind the obstacle leads to bubble coalescence. But bubbles of larger bubble diameter are experiencing different bubble drag and therefore are able to escape from the vortex due to buoyancy. This leads to the smaller peak air volume fraction in the vortex core behind the obstacle which can be observed in the experiment.

Furthermore the plot in Fig. 9 is showing the flow stagnation upstream of the obstacle and the area of reduced air volume fractions at the left pipe wall, which is due to the strong flow acceleration in the gap between the obstacle and the pipe wall. Development of air volume fraction distributions in the non-obstructed area of the pipe is showing a near wall maximum in the air volume fraction as well as the change in volume fraction distribution due to flow reattachment to the pipe wall. Both observations are comparing fairly well to the experimental observations from the wire-mesh sensor data.

Furthermore CFD data show a small bubble free region downstream of the obstacle close to its surface, which is caused by the stagnation point of the flow recirculation on the obstacle surface in interaction with the finite bubble rise velocity due to buoyancy. For test case conditions 074 this region is too small to show up in the wire-mesh sensor data with their limited spatial resolution in axial direction. But a similar bubble free region on the upper obstacle surface could be observed for other test case conditions with reduced superficial water velocity (see Fig. 6).

A more detailed 3-dimensional comparison between CFD and experimental data can be obtained from Fig. 10 by drawing from both data sets an isosurface at 4% air volume fraction. As can be seen from the figure, the 3-dimensional shape and the axial extension of high air volume fraction regions are very similar both for the wake region downstream the obstacle and for the near wall regions, where a local near wall maximum of the air volume fraction occurs due to acting lift forces for the given bubble sizes.

Fig. 11 shows a similar comparison of both data sets at the symmetry plane for the absolute value of the vertical component of the water velocity (since the sign of the water velocity can not be obtained from wire-mesh sensor data). The comparison clearly shows the nearly identical location for the vortex core (zero velocity) and for the maximum downward directed velocity in the vortex due to recirculation. Furthermore the figure shows the strong fluid acceleration in the narrow gap between the pipe wall and the obstacle as well as the fluid acceleration in the non-obstructed area of the pipe. The later seems to be a little bit underpredicted by the marker bubble approach used for the derivation of the water velocity component from the wire-mesh sensor data, since it has to be kept in mind that the water velocity is not a directly measured quantity in this case. The reattachment length of the flow behind the obstacle is again quite comparable for both CFD and experimental data, also is seems to be a little bit shorter in the experiment.

By plotting air volume fraction at individual measurement cross sections from z=-520mm to z=+520mm it was observed, that experimental data show at higher elevations (e.g. z=+40mm to z=+250mm) regions of very low air volume fraction in the non-obstructed area of the pipe, while very pronounced "hot spots" of high air volume fraction values exist close to the x=0mm location downstream of the straight edge of the obstacle. Fig. 13 shows cross-sectional plots of both the numerically predicted and experimentally measured air volume fractions for the measurement cross-sections downstream the obstacle, where this phenomenon of lateral demixing of air volume fraction can be observed. For selected cross-sections at z=+20mm, z=+80mm and z=+160mm enlarged plots for the CFX simulation results and wire-mesh sensor air volume fraction measurements can be found in Fig. 14. It was already discussed, that the air volume fraction accumulation in the

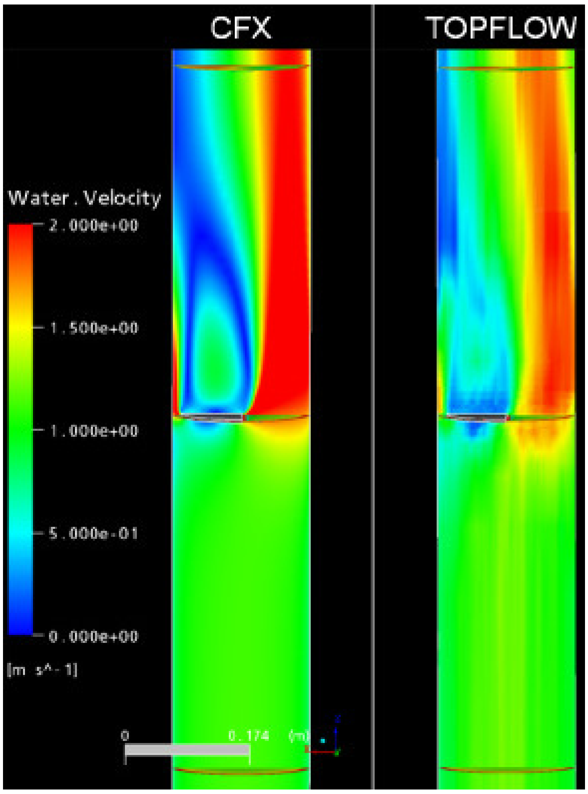


**Figure 11:** Measured and predicted absolute water velocity distribution in the symmetry plane of the flow geometry for -500mm≤z≤500mm.

recirculation area downstream the obstacle is quantitatively different in CFD and experiment due to the locally constant bubble diameter assumed in the CFX simulations and resulting buoyancy effects.

Therefore different colour scaling has been applied to the air volume fraction plots in Fig. 13 and 14. But nevertheless cross-sectional distributions of CFD and experimental air volume fractions show very similar patterns and maxima of air volume fraction in almost identical locations. The clearly reduced air volume fraction in a sharply marked off area in the non-obstructed part of the pipe flow (in Fig. 14 on the left hand side of the plots) can be observed in both of the corresponding CFD and measurement data plots. The reason for this reduced air volume fraction in the non-obstructed part of the pipe flow is probably threefold: a) it is due to the acceleration of the fluid flow in the non-obstructed part of the pipe, b) on higher elevations z≥+40mm it is due to the cross-sectional secondary flow field of the carrier phase caused by the vortex system behind the obstacle and c) it is due to entrainment of air bubbles into the recirculating flow and acting lift forces. Especially the second factor can be clearly observed from the plotted lateral air velocity field vectors on Fig. 14b) and c), where the secondary lateral motion of air bubbles is directed towards the vortex core of the flow recirculation downstream of the obstacle. On the other hand Fig. 14a) clearly shows the stagnation point of the downward, towards the obstacle surface directed flow recirculation and the outward flow along the obstacle surface, leading to a more uniformly distributed air volume fraction in the right part of the pipe downstream the obstacle.

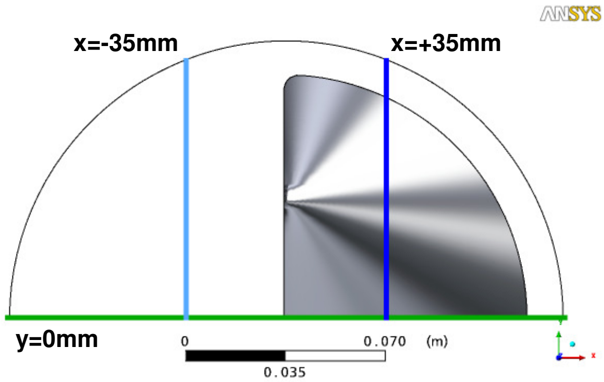


**Figure 12:** Defined cross sections for quantitative data comparison.

Furthermore, the measured air volume fraction $r_G$ and the absolute value of the axial water velocity component $|W_F|$ were quantitatively compared to the ANSYS CFX simulation results at different pipe elevation levels and for 3 different cross sections (see Fig. 12). Data have been compared at a line cross section in the symmetry plane (y=0mm) and along two different line cross sections at x=±35mm in the obstructed and non-obstructed part of the pipe. For better quantitative comparison the measured and predicted air volume fractions have been normalized against the cross-sectional averaged air volume fraction:

$$r_G\big|_{norm} = \frac{r_G}{\langle r_G \rangle_\Sigma} \tag{16}$$

Fig. 15a and 15b show the air volume fraction and axial water velocity profiles at the most upstream measurement location at z=-520mm. From these diagrams it can be seen, that the initially made CFD assumption about a fully developed two-phase bubbly flow approaching the obstacle is fairly well satisfied. The measured air volume fraction profiles show the well known near wall maximum, as it is typical for an air-water upward pipe flow with the given bubble diameter.

In Figs. 15c and 15d a first influence of the obstacle on the approaching bubbly flow can be observed. The flow is accelerating in the non-obstructed part of the pipe (on the left of Fig. 15d and is stagnating in front of the obstacle. Next diagrams from Fig. 15 show the further downstream flow development after the bubbly flow has past the obstacle. Axial water velocity profiles in Figs. 15f and 15h clearly show the flow recirculation behind the obstacle, where the axial water velocities originally show negative values. It can be seen, that the wire-mesh sensor is not able to exactly predict the sign change in axial water velocities (location of zero water velocity), which gives a raw estimate for the accuracy of the measurement in regions of low velocity values. Close to the pipe wall at x=+98mm the strong acceleration of the fluid in the narrow gap between the obstacle and the pipe wall can be observed, which is overpredicted in the CFD results due to the limited mesh

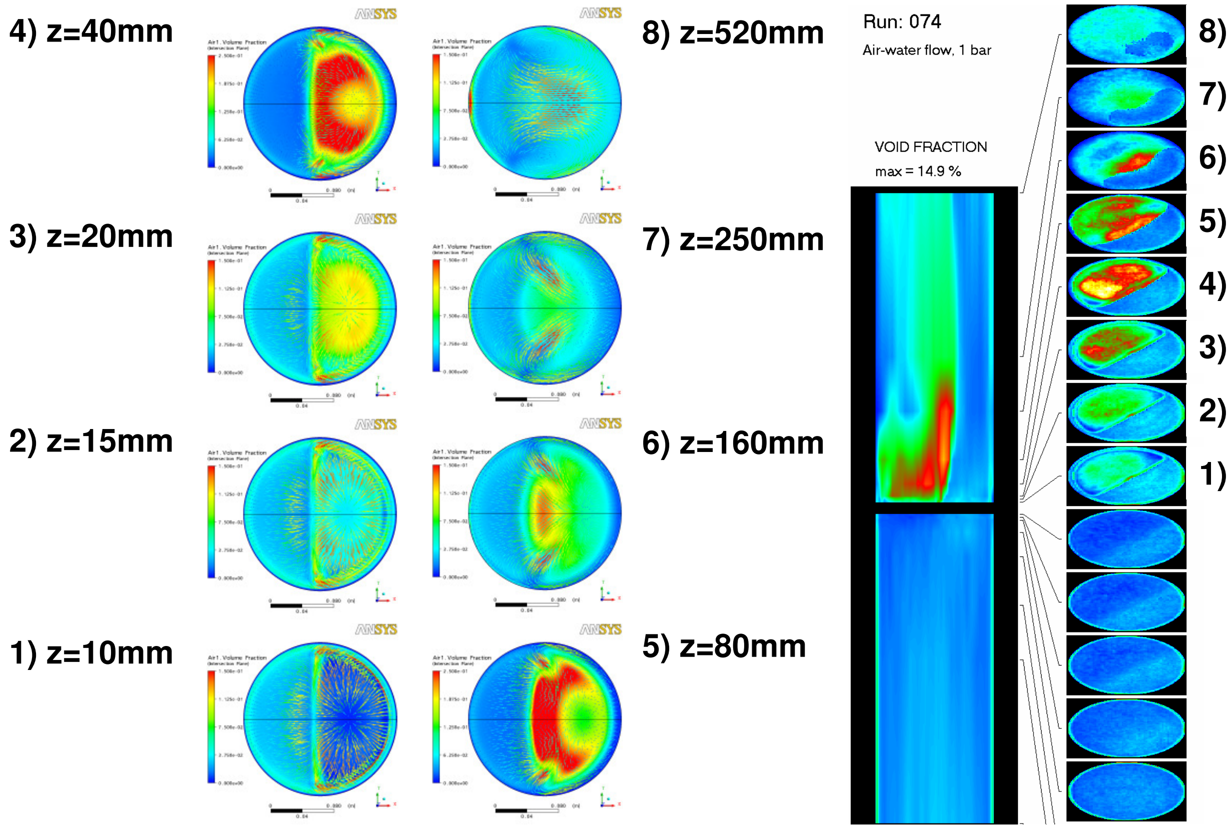


**Figure 13:** Comparison of cross-sectional air volume fraction distributions for measurement cross sections at z=+10mm to z=+520mm downstream of the obstacle. CFD data on the left hand side show additionally the normalized lateral air velocity vectors.

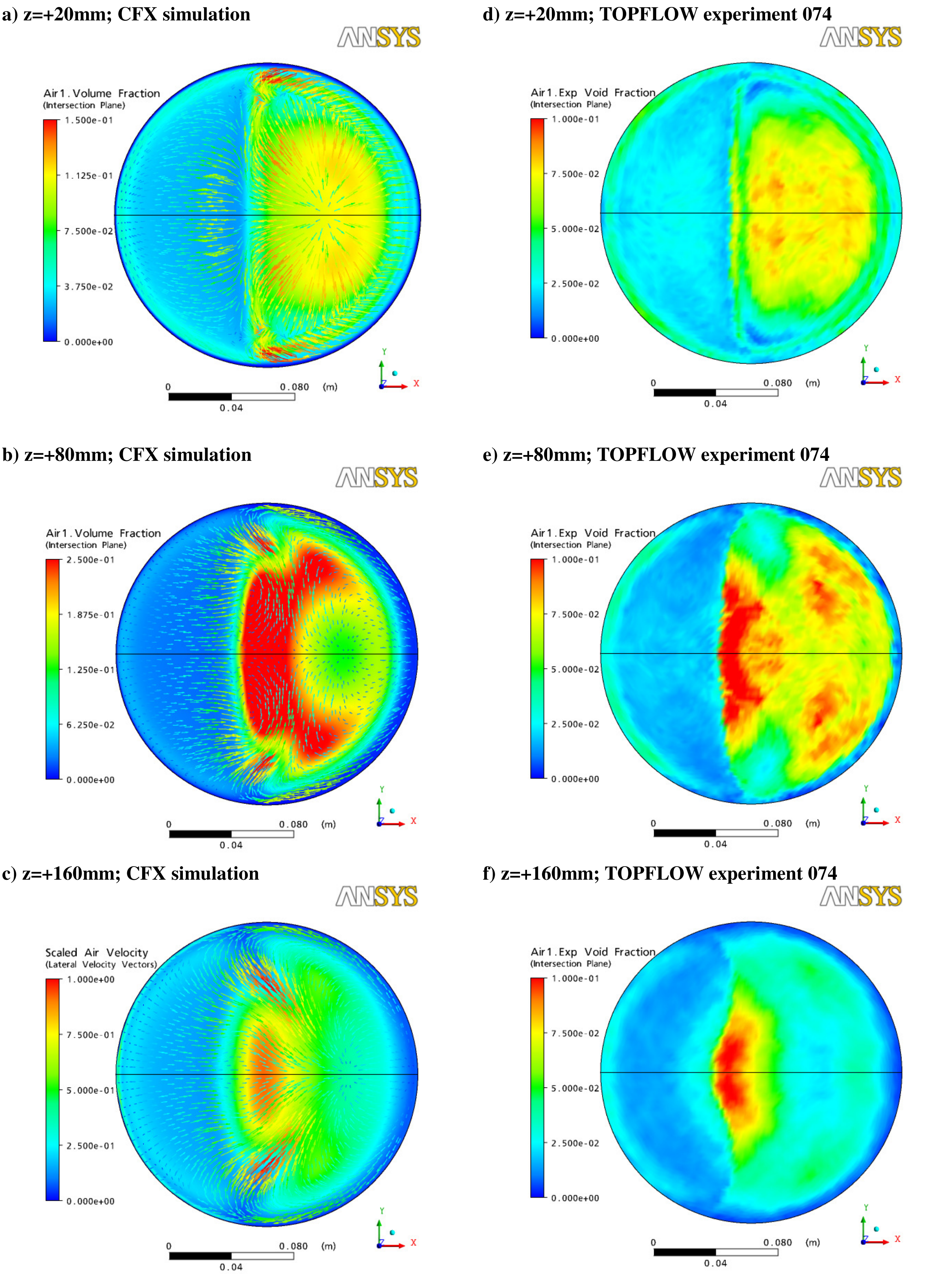


**Figure 14:** Air volume fraction distribution and normalized lateral air velocity fields (x-y-components of air velocity vector) for cross sections at measurement locations a) z=+20mm, b) z=+80mm and c) z=+160mm as predicted from ANSYS CFX simulation. Figures d), e) and f) show the wire-mesh sensor data for the air volume fraction at z=+20mm, z=+80mm and z=+160mm correspondingly (please mention the different color scaling used in corresponding plots).

**a) z=-520mm:**

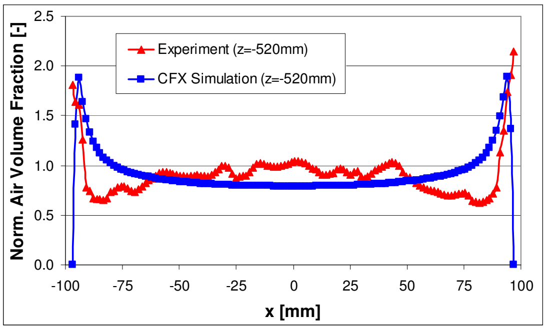


**b) z=-520mm:**

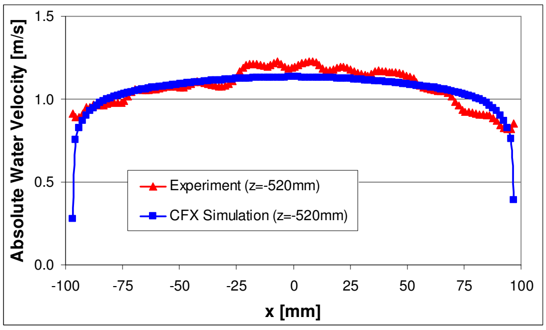


**c) z=-20mm:**

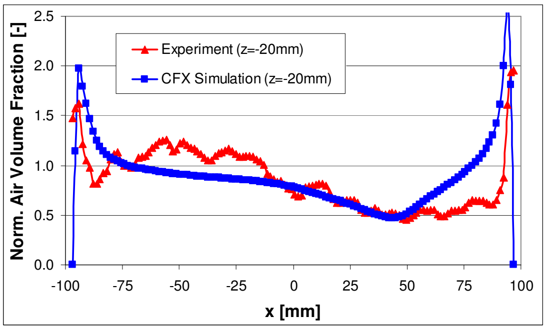


**d) z=-20mm:**

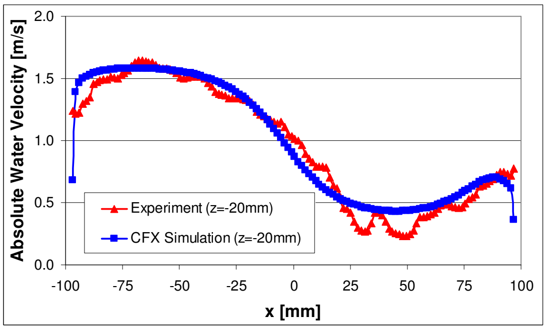


**e) z=+20mm:**

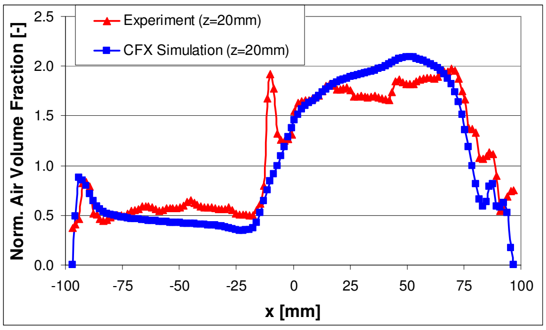


**f) z=+20mm:**

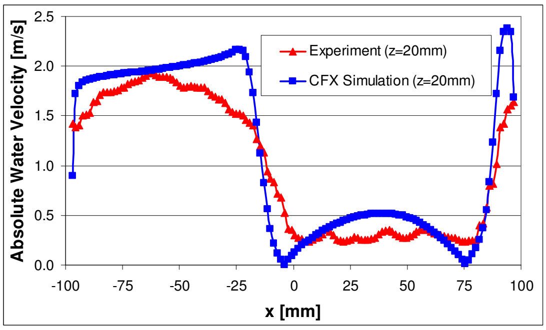


**g) z=+80mm:**

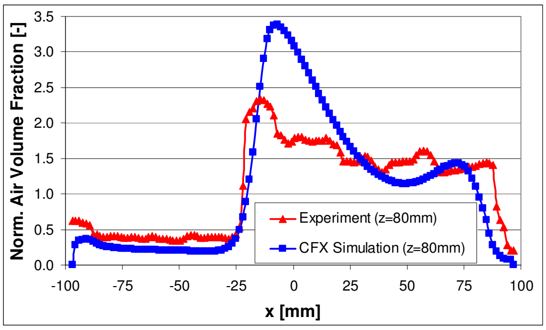


**h) z=+80mm:**

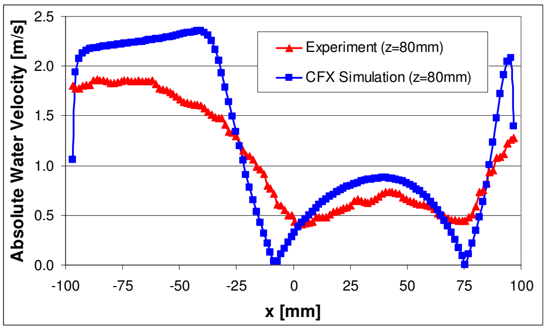


**i) z=+250mm:**

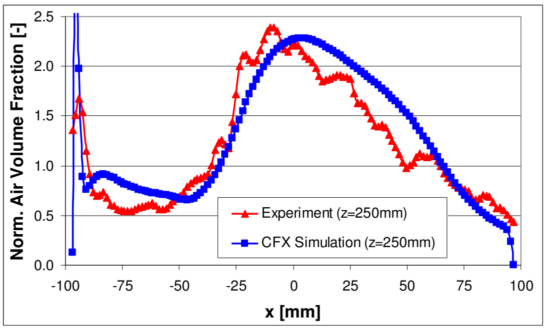


**j) z=+250mm:**

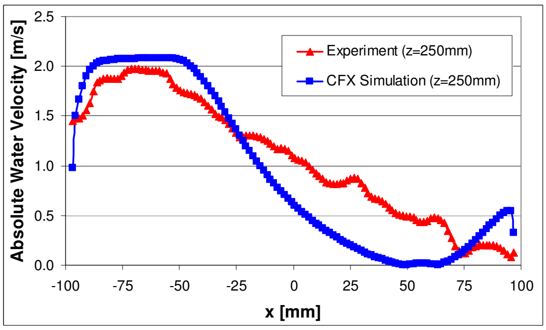


**Figure 15:** Comparison of normalized air volume fraction and absolute value of vertical water velocity at line cross section in the symmetry plane (y=0mm) for measurement cross sections at different pipe elevation.

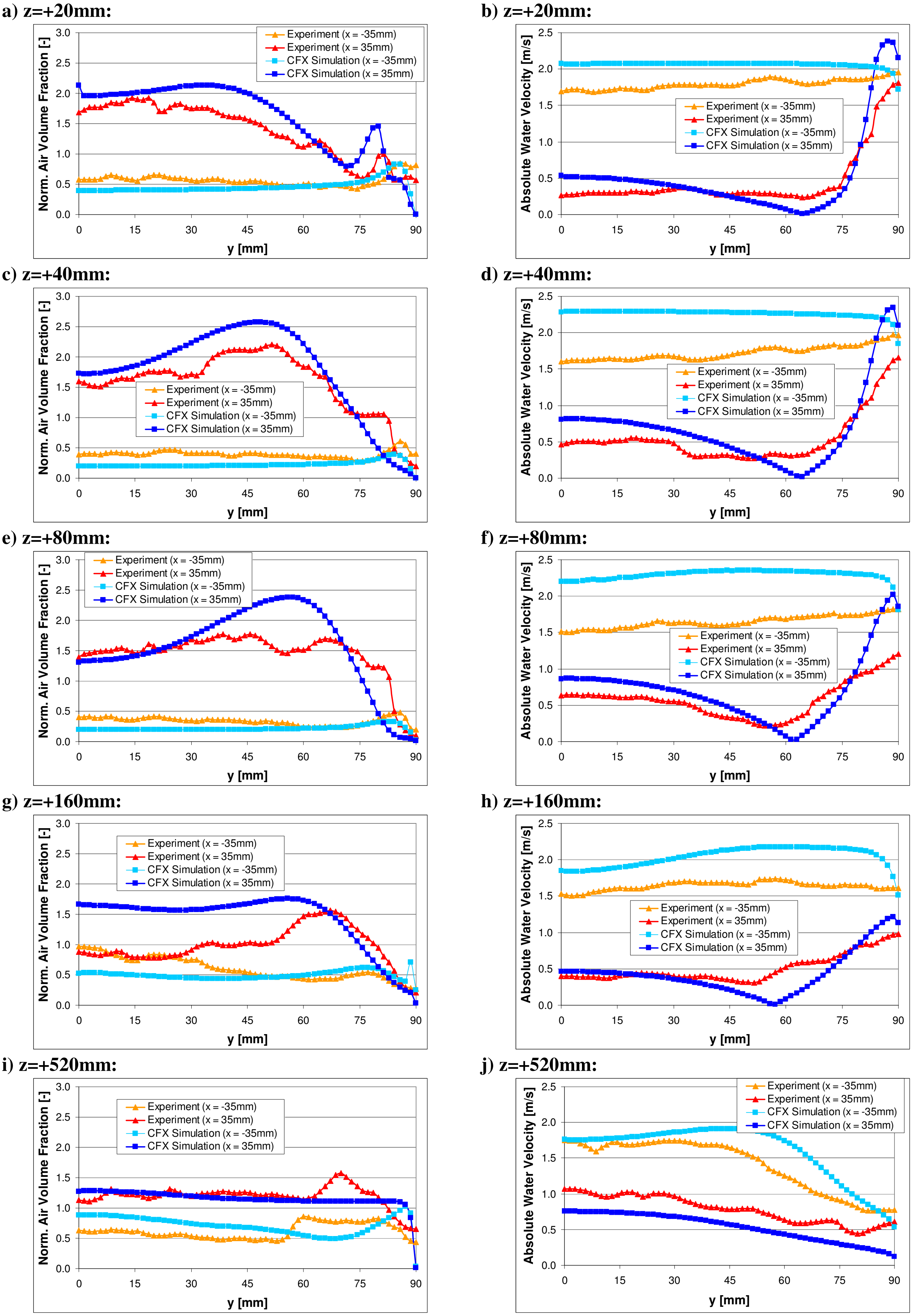


**Figure 16** Comparison of normalized air volume fraction and absolute value of axial water velocity at line cross sections x=±35mm for measurement cross sections downstream of the obstacle.

resolution on the given level of mesh refinement. On the other hand similar slightly overpredicted axial velocities can be observed in the non-obstructed region of the pipe on the left of the diagrams (x<0mm). The air volume fraction profiles in Figs. 15e, 15g and 15i are in general good agreement to the experimental values, also Fig. 15g shows an overpredicted maximum of the normalized air volume fraction downstream of the straight edge of the obstacle. Finally it can be observed that at z=+250mm both the air volume fraction and the skewed axial water velocity profiles are in very good agreement again between CFD results and experiment.

Fig. 16 shows the comparison of the same physical properties along line cross sections at x=±35mm for measurement locations downstream of the obstacle. Again axial water velocity profiles in Figs. 16b, 16c, 16f and 16h show the downward directed flow recirculation in the vortex behind the obstacle (for x=+35mm), while the axial water velocities in the non-obstructed part of the pipe (x=-35mm) seem to be slightly overpredicted in the CFD simulation. Again the flow acceleration in the narrow gap between the obstacle edge and the pipe wall at y~80-90mm is overpredicted in the CFD result as well, again due to limited mesh resolution. Air volume fraction profiles along the line cross sections x=±35mm are in generally good agreement between CFD and experiment. The accumulation of air volume fraction in the recirculation area downstream the obstacle is overpredicted in the CFD result for cross sections z=80mm and z=160mm, which can be addressed to the bubble coalescence effects taking place in the real flow. These lead to the formation of larger air bubbles in the area of higher air volume fractions and in turn these larger air bubbles are able to escape from the recirculating vortex due to buoyancy and thus reducing the local maximum air volume fraction. Finally at z=+520mm the air volume fraction profiles show an almost homogenized air volume fraction distribution, also the air volume fraction level is still higher downstream of the obstructed part of the pipe (for x=+35mm) and axial water velocity is still higher downstream the non-obstructed part (for x=-35mm).

## 6. Conclusions

A novel technique to study the two-phase flow field around an asymmetric diaphragm in a vertical pipe is presented, that allows to produce data for CFD code validation in complex geometries. Main feature is a translocation of the diaphragm to scan the 3D void field with a stationary wire-mesh sensor. Besides time-averaged void fraction fields, a novel data evaluation method was developed to extract estimated liquid velocity profiles from the wire-mesh sensor data. The flow around an obstacle of the chosen geometry has many topological similarities with complex flow situations in bends, T-junctions, valves, safety valves and other components of power plant and other industrial equipment and flow phenomena like curved stream lines, which form significant angles with the gravity vector, flow separation at sharp edges and recirculation zones in their wake are present. It is the goal of the ongoing CFD code development for ANSYS CFX to accurately model such phenomena in a two-phase flow. Therefore, the experiments provide a good basis for testing, verification and the validation of the codes and their underlying multiphase flow and turbulence models. Due to the generalizing capability of CFD codes, that can adapt to different geometric boundary conditions by the mesh generation. A successful validation on the kind of obtained experimental data guarantees the applicability of the code to other equally complex flow fields.

A pre-test calculation done by ANSYS CFX using an Eulerian two-phase flow model based on a monodisperse bubbly flow assumption resulted in a good agreement with the experiment in terms of all significant qualitative details of the void fraction and velocity distributions. The structure and the geometry of the entire flow field in general as well as the dimensions of recirculation and stagnation zones in particular were predicted in good agreement with the experiment. An import of the 3-dimensional fields of experimental data into the ANSYS CFX post-processor allowed for quite unique and detailed analysis and quantitative comparison of the CFD results with experimental data at arbitrary locations between measurement planes at z=-520mm and z=+520mm up- and downstream the obstacle.

The fact that for the time being a simple monodisperse bubbly flow was assumed, lead to an overestimation of void fractions especially in the wake of the obstacle, while the velocity profiles are matching better. It is planned to continue with post-test calculations in order to achieve a better quantitative agreement by using measured bubble-size distributions from the region upstream of the obstacle as inlet boundary condition and in a further step by applying the inhomogeneous MUSIG model for the prediction of bubble size distribution and bubble coalescence. The experimental data will be used to validate this recently developed and implemented model against detailed bubble size and bubble scale resolved void fraction measurements.

## Acknowledgements

The work was carried out in the framework of research projects funded by the German Federal Ministry of Economics and Labor, project numbers 150 1265 and 150 1271. The authors furthermore express their gratitude to the TOPFLOW technical team.

## References

1. Schaffrath A., Krüssenberg A.-K., Weiss F.-P., Hicken E. F., Beyer M., Carl H., Schuster J., Schuetz P., Tamme M.: "TOPFLOW - a new multipurpose thermalhydraulic test facility for the investigation of steady state and transient two-phase flow phenomena", Kerntechnik, 66 (2001) 4, pp. 209-212 (2001).
2. Prasser, H.-M., Beyer, M., Böttger, A., Carl, H., Lucas, D., Schaffrath, A., Schütz, P., Weiss, F.-P., Zschau, J.: "Influence of the pipe diameter on the structure of the gas-liquid interface in a vertical two-phase pipe flow", Nuclear Technology 152 (2005) 10. pp. 3-22 (2005).
3. Prasser H.-M., Beyer M., Böttger A., Carl H., Lucas D., Schaffrath A., Schütz P., Weiß F.-P., Zschau J.: "TOPFLOW Tests on the Structure of the Gas-Liquid Interface in a Large Vertical Pipe", Jahrestagung Kerntechnik 2004, Düsseldorf, 25.-27. Mai 2004, pp. 69 – 74 (2004).
4. Prasser H.-M.: "Influence of the Gas Injection on the Void Fraction Profiles and Bubble Size Distributions of a Air-Water Flow in Vertical Pipes", 5th ICMF'04,

Yokohama, Japan, May 30–June 4, 2004, #187.
5. Prasser H.-M., Beyer M., Carl H., Pietruske H., Schütz P.: "Steam-water experiments at high pressure to study the structure of the gas-liquid interface in a large vertical pipe", Annual Meeting on Nuclear Technology, Nuremberg, May 10-12, 2005, paper 215 (2005).
6. Frank Th.: Final Report in GRS-BMWA Project No. 150-1271 "Development of CFD Software for the simulation of multi-dimensional flows in the reactor cooling system", ANSYS Technical Report ANSYS/ TR-06-01, pp. 1-72, January 2006.
7. Frank Th., Zwart P.J., Krepper E., Prasser H.-M., Lucas D.: "Validation of CFD models for mono- and polydisperse air-water two-phase flows in pipes", CFD4NRS Workshop on Benchmarking of CFD Codes for Application to Nuclear Reactor Safety, OECD/NEA International & International Atomic Energy Agency (IAEA) Workshop, GRS, Garching, Germany, 5.-7. September 2006, pp. 1-19 (to be published in Nucl. Eng. Design, 2007).
8. Pietruske H., Prasser H.-M.: "Wire-mesh sensors for high-resolving two-phase flow studies at high pressures and temperatures", NURETH-11, Avignon, France, Oct. 2-6, 2005, #533 (2005).
9. Prasser H.-M., Scholz D., Zippe C.: "Bubble size measurement using wire-mesh sensors", Flow Measurement and Instrumentation, 12/4, pp. 299-312 (2001).
10. ANSYS CFX 11.0 Users Manual, ANSYS Inc., January 2007.
11. Frank Th., Shi J., Burns A.D.: "Validation of Eulerian multiphase flow models for nuclear reactor safety applications", 3rd TPFMI, Pisa, 22.-24. Sept. 2004, pp. 1-8 (2004).
12. Tomiyama A.: "Struggle with computational bubble dynamics", ICMF'98, 3rd Int. Conf. Multiphase Flow, Lyon, France, pp. 1-18, June 8.-12. 1998.
13. Antal S.P., Lahey R.T., Flaherty J.E.: "Analysis of phase distribution in fully developed laminar bubbly two-phase flow", Int. J. Multiphase Flow, Vol. 7, pp. 635-652 (1991).
14. Tomiyama A.: "Single bubbles in stagnant liquids and in linear shear flows", Workshop on Measurement Technology (MTWS5), FZ Rossendorf, Dresden, Germany, 2002, pp. 3-19 (2002).
15. Lucas D., Krepper E., Prasser H.-M.: "Development of co-current air-water flow in vertical pipe", Int. J. Multiphase Flow, Vol. 31, pp. 1304-1328, 2005.
16. Prasser H.-M., Beyer M., Carl H., Gregor S., Lucas D., Schütz P., Weiss F.-P.: "Evolution of the Structure of a Gas-Liquid Two-Phase Flow in a Large Vertical Pipe", The 11th International Topical Meeting on Nuclear Reactor Thermal-Hydraulics (NURETH-11), Popes Palace Conference Center, Avignon, France, October 2-6, 2005.